Gas-Liquid Flows Through Porous Media in Microgravity: The International Space Station Packed Bed Reactor Experiment

Brian J. Motil*[a], Enrique Ramé[b], Paul Salgi[c], Mahsa Taghavi[c] and Vemuri Balakotaiah[c]

[a]NASA Glenn Research Center, Cleveland, OH, USA

[b]USRA at NASA Glenn Research Center, Cleveland, OH, USA

[c]Department of Chemical and Biomolecular Engineering, University of Houston, Houston TX, USA

Abstract

Experimental results on pressure drop and flow patterns for gas-liquid flow through packed beds obtained in the International Space Station with two types of packing are presented and analyzed. It is found that the pressure drop depends on the packing wettability in the viscous-capillary (V-C) regime and this dependence is compared with previously published results developed using short duration low-gravity aircraft tests. Within the V-C regime, the capillary contribution is the dominant force contributing to the pressure drop for the wetting case (glass) versus the viscous contribution dominating for the non-wetting case (Teflon). Outside of the V-C regime, it is also found that hysteresis effects that are often strong in normal gravity gas-liquid flows are greatly diminished in microgravity and pressure drop is nearly independent of packing wettability. A flow pattern transition map from bubble to pulse flow is also compared with the earlier aircraft data.

Keywords: viscous-capillary regime, bubbly flow, pulse flow, microgravity, pressure drop

---

* Corresponding author

Introduction

The Packed Bed Reactor Experiment (PBRE) was developed and flown on the International Space Station (ISS) by NASA to extend a series of fundamental studies of gas-liquid flows through porous media. Flow through porous materials for space applications are encountered in life support systems, fuel cells, chemical/materials processing and transporting nutrients to plants. These systems operate differently in the microgravity environment encountered in space because the density differences no longer cause the phases to separate or "drain" under the body force of gravity. In the absence of gravity, the interfacial or capillary forces play a more significant role in determining the operational variables such as phase distribution, liquid holdup, and pressure drop. This is most apparent when the liquid inertia and viscous forces are minimal. This is the case for most of the space processes mentioned above, i.e. lower liquid flow rates and use of air/water systems.

The goals of this experiment were to better understand and improve upon the design and operation of space-based porous media flows where both gas and liquid phases are present. During the early days of the ISS assembly, NASA identified the need to conduct a series of parabolic aircraft flights to develop a semi-empirical prediction for pressure drop and flow pattern transition for two-phase flows through porous media[1] in anticipation of a number of reactor beds planned for water reclamation processes. These experiments included a range of packing sizes, column diameters, and liquid viscosities. However, important limitations to the aircraft flights included only a short time interval of low gravity (~ 20 sec) followed by a high gravity "pull-up" of the aircraft which quickly drained the vertically oriented test section. Unfortunately, the range of flow rates typical in water reclamation processes takes several minutes to fully develop into steady flow conditions. Table 1 illustrates the range of steady flow rates (superficial mass fluxes) for an air-water/glycerin system on the aircraft compared to the range available on the ISS. It is important to note, the aircraft experiment extended the range of dimensionless parameters by increasing the liquid viscosity through the addition of glycerin (up to 20 cP) whereas the ISS experiment used pure water exclusively but was able to achieve steady flows at much lower flow rates (L and G).

In this work, we describe the experimental apparatus flown on the ISS and then present and compare the results to the semi-empirical modeling approach developed based on aircraft flights. The observed pressure drop and flow transitions are discussed as well as the effect of a non-wetting packing material (Teflon). The results of additional experiments conducted to study the effects of transient flows, i.e. sequentially increasing and decreasing the flow rate of either the gas or liquid phase while holding the other constant are also discussed.

Experiment Setup and Procedure

The PBRE was designed to deliver a wide range of tightly controlled gas (nitrogen) and liquid (water) flows to one of two interchangeable test sections differing only in the type of internal packing material. Each cylindrical test section was 60 cm long and 5.08 cm in diameter. The test section columns were constructed out of clear Lexan polycarbonate for flow visualization and each column was filled with 3 mm spherical beads. The randomly distributed beads were held or “fixed” in place by spring-loaded perforated end caps. One column was filled with (wetting) glass spheres, the other with (non-wetting) Teflon spheres in order to compare the effect of the wetting characteristics of the packing material on pressure drop and flow distribution.

The basic flow loop (Figure 1) consisted of an external nitrogen supply line (supplied by the ISS) which was separated from the water downstream of the test section and then vented back into the cabin. The water was collected in the separator and recirculated in a closed-loop fashion. Multiple gas and liquid loops were required for each phase (two each) to accurately measure and control the full range of flow rates provided in Table 1. After selecting the appropriate loop, gas and liquid were mixed in a manifold or mixing chamber attached to the inlet of the test section. The gas and liquid flowed concurrently through the test section and exited through a common pipe that led to a cyclonic phase separator, required for separating the phases in low gravity.

The overall system pressure was regulated and recorded through the separator gas vent. In the steady flow test runs discussed in this paper, the regulator was open to the cabin pressure (no additional back pressure) which was generally around 100 kPa. System temperatures were recorded but not actively controlled. Since the controlling electronics were integrated closely with the flow loop, some heat was absorbed into the fluid loop and the water temperature would rise slowly over the duration of several hours of operation. The temperature rise during a single test run was negligible, i.e. less than 1 deg. C. Testing was terminated if the water temperature exceeded 30 degrees Celsius. Instrumentation for the PBRE involved measuring flow rates, temperatures, pressures and recording video. Five absolute pressure transducers with an accuracy of +/- 0.14 kPa, spanned the entire column length at equally spaced intervals (Figure 2) to record pressure measurements at a rate of 1000 Hz. Temperatures and pressures were measured at each fluid inlet line just upstream of the mixing chamber, and at the exit of the test section. Two high-speed video cameras were focused on two 10 cm segments along the test section length. One segment was located at the column inlet and the other was near the middle of the test section (Figure 2). Each camera was equipped with a parfocal, 6X zoom capable lens with a field of view from 74.4 mm to 12.5 mm in the axial direction. A variable video frame rate was selected up to a maximum of 150 frames per second. A set of controlled LED strobe lights were used for illumination to improve stopping action (minimize individual image blur).

Two pumps were used to deliver the water to the test section, a low flow pump for flow rates not exceeding 12 l/hr and a high flow pump for flow rates above 12 l/hr. The main gas line delivered the entire range of flow rates indicated in Table 1 through the use of two mass flow controllers, one for high gas flow (above 0.02 kg/hr) and the other for low gas flow (not exceeding 0.02 kg/hr). In addition, gas could also be delivered through either or both needles embedded directly inside the packing and located near the wall surface in the upstream camera's field of view (Figure 2).

For the steady flow experiments, the column was first flushed with liquid at 150 l/hr for 30 seconds. Another flush with liquid at 20 l/hr was then performed for an additional 2 minutes to establish a common initial liquid holdup state. The gas and liquid flow rates were subsequently set to the desired values and the two phases were allowed to flow for a sufficiently long period of time (estimated at about twice the time required for the phases to travel through the column) before data collection was initiated. Pressure data were then recorded for a period of 30 to 40 seconds and a video of 4 to 8s was captured at both camera locations. In addition to steady flow conditions, a series of transient experiments were also conducted by starting with the same liquid flush sequence as those carried out in the steady flow runs. For the transient runs, the gas flow was held fixed at various constant rates while the liquid flow was increased through a series of steps and then decreased in the same manner. Similarly, the liquid was held at fixed flow rates while the gas flow was increased and decreased. In constant gas (liquid) runs, the gas (liquid) flow rate was set to the desired value following the liquid flushes while the other phase was gradually increased then decreased between the low and high limits. Pressure and video data were recorded at each intermediate liquid (gas) flow rate. The purpose of these experiments was to check for the presence of hysteresis in the pressure drop versus flow rates.

Experimental Results on Pressure Drop

General Considerations

For glass spheres, a total of 495 steady-state test points were obtained, which included 28 runs with gas injection through the needles. These test points were obtained during three separate series of experiments. The same experimental protocol was followed in all three series. For the Teflon packing, a total of 187 test points were obtained. All of these points were obtained in a single series of experiments. Transient experiments with glass spheres included 52 constant-liquid runs and 55 constant-gas runs. Similar experiments with Teflon spheres included 63 constant-liquid runs and 42 constant-gas runs. The full set of steady-state results obtained on the ISS experiment are provided in the Supplementary Material to this paper as pressure drop versus flow rates for each of the four data sets.

In the next two sections, we present the pressure drop and flow map data for both the glass and Teflon packings. Emphasis is placed on comparing the data with available microgravity correlations [1] that were previously developed based on data collected during parabolic trajectories on an aircraft which provided a low-gravity environment.

Table 1 compares the differences between the test conditions of aircraft and more recent ISS tests. The initial aircraft testing was limited by relatively short durations of microgravity (~20 sec) which required relatively high flow rates of gas and liquid to ensure steady-state prior to collecting data. However, the series of aircraft tests provided a clear advantage by allowing us to examine a number of other important parameters such as liquid viscosity, packing size, test section size, and packing material. Details are discussed in the earlier paper[1], but this allowed for a much wider range of many of the important dimensionless parameters such as liquid Reynolds and Suratman numbers. The disadvantage to the aircraft was the brevity of microgravity intervals, which led to the development of the ISS experiment. The ISS experiment enabled testing to overlap some of the earlier aircraft data for air-water systems and then extend it to much lower flow rates which are typical of actual water processing systems flown in space. Due to the high launch costs and complexity of ISS experiments, only one liquid viscosity (0.9 cP, water at ~25 deg C) was tested, but because of the much longer test durations, we were able to achieve an order of magnitude reduction in both the gas and liquid Reynolds numbers on the ISS tests when compared to the aircraft tests.

Another important difference between the aircraft and ISS testing created some unanticipated challenges. The ISS experiment used a "closed-loop" water system with a cyclonic separator. The cyclonic separator design used a second pump to recycle the water in a cylindrical tank to achieve separation of the two phases. The gas was vented, but the water was then recirculated back to the test section during each test. In contrast, the aircraft test loop had a large holding tank to collect the two phases and then separate them after the 20 second microgravity period. During the normal gravity durations of the flight, the liquid was pumped back to a supply tank which was then rapidly pressurized to provide a very steady liquid flow back to the test section. We point these design differences out because under certain flow conditions (typically mid to high water flows), pressure oscillations were observed throughout the flow loop on the ISS experiment but not during the aircraft testing, i.e. they were not caused by the test column. The oscillations were generally small and at a lower frequency than the pulse flows generated by the packed bed.

Brief Review of Aircraft Correlations (Motil et al.,2003)[1]

To provide context, we first review the aircraft correlations referred to in the previous section and provide definitions for the dimensionless numbers used in these correlations.

The two-phase friction factor is written as the sum of an Ergun-type single-phase friction factor (valid in the liquid-only limit) and a "dynamic phase interaction term" that models the complex effects of introducing a gas phase. This term is to account for the forces resisting flow at the pore level such as capillary forces and a reduction of the area available for liquid flow due to trapped gas bubbles:

$$f_{TP} \equiv \frac{-\Delta P}{Z}\frac{d_p}{\rho_L U_{LS}^2}\frac{\varepsilon^3}{1-\varepsilon}$$

$$= \frac{1-\varepsilon}{\mathrm{Re_{LS}}}\left[C_V + C_S\left(\frac{\mathrm{Re_{GS}}}{1-\varepsilon}\right)^{1/2}\left(\frac{\mathrm{Su_L}(1-\varepsilon)}{\mathrm{Re_{LS}}}\right)^{2/3}\right] + C_I, \qquad (1)$$

where the dimensionless dynamic phase interaction term is defined by

$$\frac{1-\varepsilon}{\mathrm{Re_{LS}}}\left[C_S\left(\frac{\mathrm{Re_{GS}}}{1-\varepsilon}\right)^{1/2}\left(\frac{\mathrm{Su_L}(1-\varepsilon)}{\mathrm{Re_{LS}}}\right)^{2/3}\right] = \frac{1-\varepsilon}{\mathrm{Re_{LS}}}\left[C_S\left(\frac{\mathrm{Re_{GS}}}{1-\varepsilon}\right)^{1/2}\left(\frac{\mathrm{Re_{LS}}(1-\varepsilon)}{\mathrm{We_{LS}}}\right)^{2/3}\right]$$

$$= \frac{1-\varepsilon}{\mathrm{Re_{LS}}}\left[C_S\left(\frac{\mathrm{Re_{GS}}}{1-\varepsilon}\right)^{1/2}\left(\frac{\mathrm{Ca_{LS}}}{1-\varepsilon}\right)^{-2/3}\right]. \qquad (2)$$

The best fit constants for aircraft based data were C_V=180.0, C_I=1.8, and C_S=0.8. It should be stressed that the aircraft data used to fit Eq. (1) did not cover the regime of low gas and liquid flow rates, which is the focus of the ISS experiments.

In addition, the "transition" from bubbly to pulse flow was found to be correlated by the following expression:

$$\left(\frac{\mathrm{Re_{GS}}}{\mathrm{Re_{LS}}}\right)_{tran} = 700\mathrm{Su_L}^{-2/3}. \qquad (3)$$

In Equation 1, $-\Delta P$ is the pressure drop over the packed distance Z, d_p is the packing diameter, U_{LS} is the liquid superficial velocity, and ε is the average bed porosity. The dimensionless numbers in Equations 1 and 2 are defined as follows:

$$\mathrm{Re_{LS}} = \frac{\rho_L U_{LS} d_p}{\mu_L} \qquad \textit{Liquid Reynolds number} \qquad (4a)$$

$$\mathrm{Re_{GS}} = \frac{\rho_G U_{GS} d_p}{\mu_G} \qquad \textit{Gas Reynolds number} \qquad (4b)$$

$$\mathrm{Su_L} = \frac{\mathrm{Re_{LS}^2}}{\mathrm{We_{LS}}} = \frac{d_p \rho_L \sigma}{\mu_L^2} \qquad \textit{Suratman number} \qquad (4c)$$

The Weber and Capillary numbers in Equation 2 are defined by:

$$\mathrm{We_{LS}} = \frac{\rho_L U_{LS}^2 d_p}{\sigma} \qquad \textit{Weber number} \qquad (4d)$$

$$\mathrm{Ca_{LS}} = \frac{\mu_L U_{LS}}{\sigma} \qquad \textit{Capillary number} \qquad (4e)$$

In Equations 4a-4e, ρ, μ, and σ refer to density, viscosity, and surface tension, respectively. For a given phase, the modified Reynolds number is defined as the ratio of the Reynolds number to the fraction of solids in the column, i.e. $\mathrm{Re_{iS}^*} = \mathrm{Re_{iS}} / (1 - \varepsilon), i = L, G$.

Pressure Drop with Glass Packing Material

Results are shown in figures 3 and 4 comparing experimental pressure drop for the glass bead packing material (wetting) on the ISS with the original modified Ergun equation (1) developed using aircraft tests. Figure 3 shows three representative cases with very low gas flows over the full range of liquid flows and figure 4 provides representative cases for the higher gas flow conditions. In both figures, the results are presented as a log-log plot of the friction factor versus the modified liquid Reynolds number, Re^*_{LS}. The dotted line represents the single liquid phase only case as a reference. From these plots, it can be seen that the general form of equation 1 fits the experimental data over the full range of both gas and liquid flows but the original constants over predict the pressure drop, in particular for $Re^*_{LS} < 40$. We note that the over prediction is more pronounced for the higher Re^*_{GS} cases (Figure 4). There also is a clear transition or change in slope in all cases around Re^*_{LS} values around 40 which interestingly holds for all gas flows tested on the ISS. Finally, it is important to point out that the actual pressure drop measured during the ISS experiment is higher than predicted by the earlier aircraft correlation in the inertia regime ($Re^*_{LS} > 40$). The pressure drop data in the inertial regime will be examined in more detail in a future publication.

The transition or step increase in pressure around Re^*_{LS} of 40 ± 10 was not observed earlier on the aircraft because the lower liquid Reynolds numbers were obtained using more viscous liquids (aqueous glycerin solutions, up to 20 cP). The pure water aircraft tests with water were conducted above Re^*_{LS} values of 30 (most test points were closer to 100) and only at the higher gas flows ($Re^*_{GS} > 10$). A future test on the ISS is scheduled to better study this transition, with a focus on gas bubble entrapment. We are postulating that there is a range of moderate liquid flows that cannot flush or force trapped gas bubbles through the bed as the liquid inertia term becomes relevant. This increases the pressure drop by effectively restricting the available pore area for flow (similar to decreasing the porosity). As the liquid flow increases, the trapped gas is eventually flushed and the results approach those developed in the earlier work. This transition appears to only be a function of liquid flow rate. This is one fundamental problem identified in the PBRE, i.e. there is a minimum liquid superficial flux needed to dislodge trapped bubbles in a porous medium. If it is assumed that the dominant forces acting on the bubble are due to liquid inertia and capillarity, the relevant dimensionless group is the Weber number, $We_{LS} = \frac{\rho_L U_{LS}^2 d_p}{\sigma}$. If $We_{LS} >> 1$, the inertial force will dislodge the bubble, while for $\mathrm{We}_{\mathrm{LS}}$ << 1, the bubble is stuck. Since the highest superficial velocities of the liquid used in the PBRE correspond to a Weber number that is less than unity, we conjecture that the flushing of the column by liquid (between different experiments) may not have dislodged all the bubbles and this may have impacted the observed pressure drop. Further, it is observed that the Weber number criterion is independent of the bubble size as both inertia force and capillary force increase with bubble size with their ratio remaining constant. [The inertial force is proportional to the projected area of the bubble, which for a spherical bubble increases quadratically with the bubble diameter. The capillary force acting on the bubble is proportional to the total sphere area of the bubble, which also increases quadratically with bubble diameter]. The value of the critical Weber number, which is expected to be of order unity is to be determined by future experiments and/or modeling. As can be seen from Eqs (1) and (2), for $\mathrm{We}_{\mathrm{LS}}$ >> 1, the phase interaction term becomes negligible when inertial forces dominate the pressure drop.

As discussed earlier, one of the main objectives of the PBRE was to extend test results to realistic flow rates used for reactors currently in use or under development for space (low-gravity) operations. Table 1 shows the range of tests conducted using the low gravity aircraft versus the PBRE flown on the ISS. As noted earlier, the low gravity aircraft tests were obtained by using liquid viscosities as high as 20 cP. The higher viscosities had the unintended effect of also lowering the Su_L orders of magnitude below that of typical reactors using water (~1 cP) for the liquid phase. The best-fit constant for the dynamic phase interaction term based on the earlier aircraft experiments was C_s=0.8. For the earlier aircraft tests using pure water (~1 cP), the lowest value of $\mathrm{Re}^*_{\mathrm{LS}}$ in the range of 30 which is above the fully viscous region generally considered lower than 10 for single-phase flow (Blake-Kozeny). In fact, the 0.8 constant was empirically determined using experimental data exclusively in the transition region $10 < \mathrm{Re}_{\mathrm{LS}}^{*} < 1000$ and $8 < \mathrm{Re}_{\mathrm{GS}}^{*}$. For the ISS tests, we extended steady flows down to the range of approximately 1 and 0.1 for the modified liquid and gas Reynolds numbers, respectively. Physically, this region involves liquid flows best described by Darcy's flow modified by the effect of small bubbles on the order of the pore or packing size dispersed within the liquid.

With this in mind, we focus now on the region dominated by viscous and capillary (interfacial) forces which we identify as $0.1 < \mathrm{Re}^{*}_{\mathrm{GS}} < 1$ and $1 < \mathrm{Re}^{*}_{\mathrm{LS}} < 10$. [The lower bounds defining the viscous-capillary regime are based on the range of our experiments but can be extended to zero]. Based on equation 1, it is estimated that the relative contribution of the phase interaction term is on the order of 75% and the viscous term is around 23% with the inertia term contributing no more than 2% to the overall pressure drop. Figure 5 validates the earlier "best fit" using C_S=0.6 as the leading constant for the dynamic phase interaction term (versus 0.8). For clarity, a linear plot of pressure gradient versus $\mathrm{Re}^{*}_{\mathrm{GS}}$ is now used and which also shows how well the correlation predicts the experimental data. Since the pressure gradient in the viscous-capillary regime is fairly low, there is a significant relative error introduced in the measurements, so error bars are included. [Dimensionless pressure drop (friction factor) plots with corrected phase interaction coefficient are given in Supplementary Material].

Pressure Drop with Teflon Packing Material

Similar test conditions were also conducted using a non-wetting packing bed material (Teflon). The column design and packing size were identical to the glass bead tests while flow conditions were matched closely. The very lowest flow conditions ($\mathrm{Re}^{*}_{\mathrm{LS}}$ = 1.4) for Teflon did not produce a measurable pressure drop within the limits of our instrumentation so those test conditions are dropped in the following analysis. As with the glass packing, figures 6 and 7 compare the experimental pressure drop for Teflon packing material on the ISS with the original modified Ergun equation (1) developed with wetting packing material (non-wetting tests were not conducted on the earlier aircraft tests). Figure 6 shows three representative cases for very low gas flows while figure 7 shows cases for the higher gas flows. Teflon packing behaves similar to glass, including the transition at Re^*_{LS} equal to 40 or 50 but in general, the phase interaction term appears to be less significant over all flow rates shown.

Conducting similar analysis with a focus on the region dominated by viscous and capillary forces, a phase interaction constant best fit is found to be around 0.15 (versus 0.6 for glass) as shown in figure 8. In this region, the phase interaction term only contributes on the order of 20 to 30% of the total pressure drop (versus 75% for glass), with viscous contribution dominating (at around 70%) and the inertial contribution being negligible (below 5%). We also note that the absolute value of the pressure gradient in this regime is lower by about a factor 2 compared to the glass packing. Thus, the wetting characteristics of the packing strongly influence the pressure gradient in the viscous-capillary regime. We conjecture that the dynamic gas (and/or liquid) hold-up is also strongly impacted by the wetting but this could not be confirmed as we have not measured these quantities. Comparing the friction factor curves of Teflon and glass (figure S-5 in SM) we observe that they are very similar with the curve for glass slightly above that for Teflon and the transition to inertial regime appears to be independent of the wetting characteristics. This is likely because the contact angle does not play a significant role in the bubbly regime in which the liquid is the continuous phase and completely wets the packing.

Hysteresis Effects in Microgravity Gas-Liquid Flows

In normal gravity co-current gas-liquid downflow, it is known that the liquid holdup depends on the relative magnitude of the capillary force compared to that of the gravitational, viscous and inertia forces. The ratio of these forces is measured by the magnitude of the Bond, Capillary, and Weber numbers, respectively. A review of the literature on normal gravity trickle-bed reactors shows that these flows exhibit multiple hydrodynamic states and hysteresis behavior. For example, increasing and then decreasing the liquid (gas) flow rate, at a fixed gas (liquid) flow leads to different values for the liquid holdup and pressure gradient[2-10]. It is of interest to understand this hysteresis phenomenon and the dependence of the hydrodynamic state on the bed history, initial state, or start-up procedure as it can lead to uncertainties in the design and scale-up of the reactors. The main reasons for the hysteresis in 1-g are improper wetting of the bed, the change in gas flow path and tortuosity due to change in liquid holdup and/or flow path around the particles due to capillary effects. The key variables controlling the hysteresis in 1-g are the initial state of bed in the start-up procedure (i.e. wet or dry), particle size and type, column diameter, inlet liquid distribution, presence of surfactants, and gas/liquid operating flow ranges (which determine the magnitude of the various forces).

When the draining effects of gravity are absent, any hysteresis effects can only be due to capillary, viscous and inertial effects. Thus, we expect to see diminished hysteresis effects outside of the viscous-capillary regime. This conjecture could not be verified in aircraft experiments due to the short duration of the parabolic flights. Thus, one objective of the PBRE experiment was to examine the hysteresis effects within the range of flow conditions shown in table 1 and compare the same with normal gravity results.

A comparison between normal gravity and microgravity pressure gradient versus liquid flow rate at a constant gas flow rate is shown in Figure 9. This figure shows the existence of hysteresis at high gas flow rates (>750 kg/m^2.hr) in normal gravity reported experiments. However, in our microgravity experiments for both glass and Teflon packing, a very small amount of hysteresis effect in the measured pressure gradient was found over the range of studied flow conditions. Therefore, it may be concluded that in microgravity, the pressure gradient is nearly independent of the packing wettability outside of the V-C regime. This is shown clearly for glass packing in Figures 10a and 10c for constant gas runs and constant liquid runs, respectively. Similarly, these are presented for Teflon packing in Figures 10b and 10d. Due to the lack of enough accurate hysteresis data in the V-C regime, we could not observe hysteresis effects in this regime. However, Figures 5 and 8 verify the significant effect of the packing wettability on the pressure gradient in this regime. Thus, we conclude that hysteresis effects are negligible in microgravity for gas-liquid flows outside of the V-C regime. Within the V-C regime, hysteresis effects may be present but our pressure drop data are not accurate enough to detect them.

Flow Pattern Transition and Evolution to Pulsing

In this section, we discuss briefly the two main observed flow patterns (bubble and pulse), the transition boundary, and compare the same with data obtained in aircraft experiments.

Flow Map

The flow pattern data presented here are based primarily on video observations at the mid-section Camera 2 location (Figure 2), and power spectral density (PSD) analysis. The data are limited to liquid fluxes at or above 4 kg/m^{2}s for the glass column and 7 kg/m^{2}s for the Teflon column. These values correspond approximately to the lowest flow rate at which pulsing behavior was observed within the range of gas flow rates covered in the experiments (Table 1). The observed flow patterns are best described as “apparent flow patterns” since they correspond to rather localized near-surface observations taken over a relatively short period of time (4 to 8 seconds). We distinguish between two overall patterns, namely, bubbly flow and pulse flow. The former refers to a pattern in which the moving gas is observed to flow in discrete bubbles within the liquid continuous phase, which cover a wide range of sizes/shapes and may undergo break-up/coalescence, while the latter refers to a pattern where clear pulsations of alternating gas-rich and liquid-rich segments are observed moving across the camera's field of view. The results presented in this section can be grouped into two main categories: (i) a comparison of the experimental flow maps with the aircraft correlation[1], and (ii) a qualitative description of the evolution to pulsing in different regions of the flow map.

Several methods are available in the literature for detecting the transition to a pulsing pattern in a packed bed where gas and liquid are flowing concurrently downward[11-16]. At intermediate liquid flow rates, the transition from trickle to pulse flow may be detected by either visual inspection or other methods based on the time series analysis of pressure fluctuations at a fixed location near the bottom of the column. These methods are based on indicators such as (i) a sudden increase in the standard deviation of the pressure fluctuations, (ii) a sudden increase in the intensity of a frequency component in the power spectrum (typically in the range of 0 to 2 Hz), (iii) the emergence of a clearly defined correlation dimension for the attractor reconstructed from the pressure fluctuation time series, and (iv) the appearance of a maximum for a Hurst-like exponent resulting from an analysis of rescaled range[17]. In comparison, fewer studies address the bubble to pulse transition that occurs in 1-g at higher liquid flow rates when both the liquid and gas are flowing downward in the packed bed. Such a transition is also observed over a range of liquid flow rates in packed columns with upward co-current flow[18] and in columns operating under microgravity conditions[1]. In these studies, the transition from a bubbly to a pulsing pattern is based typically on visual observations, although Motil et al. have also used a criterion based on the sudden increase in the intensity of selected frequency components in the power spectrum of the pressure fluctuations at a fixed location near the column exit. Though the power spectrum approach still relies on arbitrarily chosen values for the magnitude of the “sudden jumps in intensity” and requires concurrent confirmation of the transition to pulsing from visual observations, we used it here to determine the transition.

The combined visual and PSD based analysis of the PBRE flow transition map is shown in figure 11. For glass spheres, data are reasonably consistent with the aircraft correlation[1]. As shown in Figure 11, at low liquid flux, pulsing in the Teflon column is observed to occur at a slightly higher gas flow rate than in the glass column, while the converse appears to be the case at the highest liquid flux. We conclude that, despite the variability in the data, the aircraft correlation appears to give a fair description of the observed flow transition over the specified range of flow conditions for both the glass and Teflon packings.

Description of Bubble to Pulse Evolution

In this section, the expression “transition to pulsing” refers to the lowest gas flow rate at which pulsing is observed (in the viewing area of Camera 2) at a given liquid flow rate. When the liquid flux is decreased from its maximum value of 21 kg/m^2.s, the transition from bubbly to pulse flow takes place at increasingly lower gas flow rates, then reaches a plateau where the transition becomes rather insensitive to the gas flow rate. This plateau is reached at a liquid flux of about 11 and 14 kg/ m^2.s for glass and Teflon spheres, respectively. At the lower end, these plateau regions extend down to a liquid flux of about 4 kg/m^{2}s for glass spheres and 7 kg/m^2.s for Teflon spheres. To the left of the plateau region (lowest liquid flux), we did not observe any evolution to pulsing over the entire range of gas flux covered in the experiments (Table 1) so this region is not shown in Figure 11. To the right of the plateau region, the flow transitions from a “dispersed bubbly” pattern into a “pulsing pattern” at increasingly higher gas flow rates. In the glass column, the dispersed bubbly pattern is characterized by relatively small bubbles (of the order of the packing diameter) that are repeately squeezing through the liquid-filled pore space as they move downstream. The motion of these bubbles has a significant “transverse” velocity component with respect to the main direction of the flow. In the pulsing regime, the video observations were not clear enough to determine the nature of the flow in the intervals separating two liquid-rich pulses. However, we do observe the presence of long gas channels in these intervals, along with smaller “breakup” bubbles. For the Teflon packing, we don’t fully enter this region even at the highest liquid mass flux of 21 kg/m^{2}s, where the typical bubble size is still on the order of several packing diameters. The large bubbles seem to push their way through the liquid, drifting in the main direction of flow as if “unaware” of the presence of the packing. In the pulsing regime, the liquid-rich pulses show significantly less intimate mixing between the two phases compared to pulses in the glass column. The intervals between pulses contain long and wide gas streaks. In this high liquid flow region, power in the PSD starts to concentrate on frequency components larger than 1 Hz at the transition. As the gas flow rate is increased, these frequency components both grow in intensity and shift to higher frequency values (Figures 12a and 12b). We note that even though we analyzed the PSD for both the glass and Teflon packing, the pressure data was not sufficiently accurate to distiquish the difference in the bubbly-pulse transition when comparing the two packing materials. Video observations clearly show the pulse was weaker (i.e., the alternating gas and liquid-rich pulsations were not as well defined) for the Teflon packing.

The three distinct regions for pulsing evolution are reminiscent of the well-documented flow map for normal gravity concurrent downflow[19], with the slow transition to low-frequency pulsing from trickling flow at intermediate liquid flux and the transition from bubbly flow to higher frequency pulsing at high liquid flux. The evolution of the PSD of pressure traces along the column can help in the interpretation of video information. These power spectra contain repeatable patterns which may be helpful in interpreting flow pattern evolution along the column. Such patterns have already been examined in the case of liquid-gas flow in open pipes (see, for instance, Shaban and Tavoularis, 2014[20]). However, a full understanding of the PSD patterns, their evolution in a packed bed, and the impact of wetting characteristics on pulse properties requires a detailed analysis that will be the subject of future work.

Summary and Discussion

In this article, we have presented and analyzed the experimental data obtained aboard the International Space Station on pressure drop and flow regimes for gas-liquid flows through packed-beds in microgravity. This is the first time long duration testing of this type has been conducted in microgravity and in some cases provided guidance for future testing as discussed later in the summary. The major conclusions from the first series of testing clearly indicate that in the viscous-capillary regime covered by the experiments ($1 < \mathrm{Re}_{\mathrm{LS}}^{*} < 10 \ and \ 0.1 < \mathrm{Re}_{\mathrm{GS}}^{*} < 1$), the phase interaction (or capillary) contribution dominates the pressure drop for the wetting case versus the viscous contribution dominating in the non-wetting case. In addition, outside of the viscous-capillary regime, it is found that the pressure drop is nearly independent of the wetting characteristics, and hysteresis effects that are present in normal gravity are very weak and nearly absent in microgravity. For both the wetting and non-wetting case, the transition from viscous-capillary to inertia dominated regime occurs at $\mathrm{Re}^{*}_{\mathrm{LS}}$ of about 30 to 50, and is nearly independent of the gas flow rate within the range of our experiments ($0.1 < \mathrm{Re}^{*}_{\mathrm{GS}} < 34$). We also verified that the bubble to pulse flow transition criterion obtained using earlier aircraft data was found to be essentialy the same for the ISS experiment. Finally, video observations indicate that the pulse flow with non-wetting packing (Teflon) is weaker compared to that in the glass column.

Additional observations which we were not able to quantify due to insufficient or inaccurate data were also made during this initial set of experiments and we hope to address these during a second set currently on the ISS and planned for operation during 2020. Our video observations showed that at very low liquid flow rates, the small gas bubbles introduced at the front section of the column coalesced as they moved downstream and formed larger bubbles whose diameter was about the same as that of the column. Thus, there is strong indication that there is a "gas continuous" flow regime at very low fluxes and longer time scales, which requires further investigation. This flow regime can also be observed in normal gravity gas-liquid two-phase up-flows in packed-beds but requires that the Bond number be much smaller than unity. For example, normal gravity experiments[21] have shown that the ratio of the bubble to packing particle diameter is inversely proportional to the Bond number ($\mathrm{Bo} = \frac{\rho_L g d_p^2}{\sigma}$). In microgravity, the Bond number approaches zero indicating that the bubble diameter can be very large compared to the packing size. This flow regime and further characterization of the viscous-capillary regime are the topics of the future ISS experiment.

Acknowledgments: This work was funded by NASA Glenn Research Center (NASA grant number 80NSSC18K0813). We would also like to acknowledge the outstanding team of engineers at ZIN Technologies for designing and operating the ISS experiment.

Figure Captions

Figure 1 Schematic diagram of the ISS PBRE experimental setup.

Figure 2 Schematic diagram of the test section along with location of the cameras and pressure transducers.

Figure 3 Log-log plots of friction factor vs modified liquid Re^*_{LS} with phase interaction constant equal to 0.8 for low gas Re^*_{GS} cases using glass beads. Lower dotted line indicates predicted friction factor for single phase liquid.

Figure 4 Log-log plots of friction factor vs modified liquid Re^*_{LS} with phase interaction constant equal to 0.8 for higher gas Re^*_{GS} cases using glass beads. Lower dotted line indicates predicted friction factor for single phase liquid.

Figure 5 Pressure gradient versus modified gas Re^*_{GS} using linear scale with error bars for glass beads with phase interaction constant equal to 0.6.

Figure 6 Log-log plots of friction factor vs modified liquid Re^*_{LS} with phase interaction constant equal to 0.8 for low gas Re^*_{GS} cases using Teflon beads. Lower dotted line indicates predicted friction factor for single phase liquid.

Figure 7 Log-log plots of friction factor vs modified liquid Re^*_{LS} with phase interaction constant equal to 0.8 for higher gas Re^*_{GS} cases using Teflon beads. Lower dotted line indicates predicted friction factor for single phase liquid.

Figure 8 Pressure gradient versus modified gas Re^*_{GS} using linear scale with error bars for Teflon beads with phase interaction constant equal to 0.15.

Figure 9 Comparison of the measured pressure gradient in hysteresis experiments in microgravity with available literature data in normal gravity.

Figure 10 Measured pressure gradient in hysteresis experiments with glass packing (a, c) and Teflon packing (b, d).

Figure 11 Comparison of flow pattern map with the aircraft correlation

Figure 12 Comparison of Power Spectral Density plots for fixed liquid and varying gas flow rates.

References

1. Motil BJ, Balakotaiah V, Kamotani Y. Gas-liquid two-phase flow through packed beds in microgravity. *AIChE Journal.* 2003;49(3):557–565.
2. Kan KM, Greenfield PF. Multiple hydrodynamics states in cocurrent two-phase down flow through packed beds. *Industrial & Engineering Chemistry Product Research and Development.* 1978;17:482-485.
3. Christensen G, McGovern SG, Sundaresan S. Cocurrent downflow of air and water in a two-dimensional packed column. *AIChE Journal.* 1986;32:1677-1689.
4. Levec J, Grosser K, Carbonell RG. The hysteretic behavior of pressure drop and liquid holdup in trickle beds. *AIChE Journal.* 1988;34:1027-1029.

5. Lazzaroni CL, Keselman HR, Figoli NS. Trickle bed reactors: Multiplicity of hydrodynamic states. Relation between the pressure drop and the liquid holdup. *Industrial & Engineering Chemistry Research.* 1989;28:119-121.
6. Goto S, Gaspillot PD. Multiple hydrodynamic states in gas-liquid upflow and downflow through beds of small packings. *Industrial & Engineering Chemistry Research.* 1992;31:629-632.
7. Wang R, Mao ZS, Chen J. Experimental and theoretical studies of pressure drop hysteresis in trickle bed reactors. *Chemical Engineering Science.* 1995;50:2321-2328.
8. Maiti R, Khanna R, Nigam KDP. Hysteresis in trickle-bed reactors: A review. *Industrial & Engineering Chemistry Research.* 2006;45:5185-5198.
9. Gunjal PR, Kashid MN, Ranade VV, Chaudhari RV. Hydrodynamics of Trickle-Bed Reactors: Experiments and CFD Modeling. *Industrial & Engineering Chemistry Research.* 2005/08/01 2005;44(16):6278-6294.
10. Ravindra PV, Rao DP, Rao MS. Liquid Flow Texture in Trickle-Bed Reactors: An Experimental Study. *Industrial & Engineering Chemistry Research.* 1997/12/01 1997;36(12):5133-5145.
11. Anadon LD, Sederman AJ, Gladden LF, Rationalising MRI. Conductance and pressure drop measurements of the trickle-to-pulse transition in trickle beds. *Chemical Engineering Science.* 2008;63:4640-4648.
12. Chou TS, Worley FL, Luss D. Transition to pulsed flow in mixed-phase cocurrent downflow through a fixed bed. *Industrial & Engineering Chemistry Product Research and Development.* 1977;16(3):424-427.
13. Honda GS, Lehmann E, Hickman DA, Varma A. Effects of prewetting on bubbly- and pulsing-flow regime transitions in trickle-bed reactors. *Industrial & Engineering Chemistry Research.* 2015;54:10253-10259.
14. Horowitz GI, Cukierman AL, Cassanello MC. Flow regime transition in trickle beds packed with particles of different wetting characteristics - check-up on new tools. *Chemical Engineering Science.* 1997;52(21,22):3747-3755.
15. Urseanu MI, Boelhouwer JG, Bosman HJM, Schroijen JC, Kwant G. Estimation of trickle-to-pulse flow regime transition and pressure drop in high-pressure trickle bed reactors with organic liquids. *Chemical Engineering Journal.* 2005;111:5- 11.
16. Wang R, Mao Z, Chen J. A study of trickling-to-pulsing flow transition in trickle-bed reactors (TBR). *Chemical Engineering Communications.* 1994;127:109-124.
17. Feder J. *Fractals*. New York: Plenum Press; 1988.
18. Raghavendra Rao AV, Kishore Kumar R, Sankarshana T, Khan A. Identification of flow regimes in a concurrent gas liquid upflow through packed beds. *Chemical Engineering and Technology.* 2011;34:1909:1917.
19. Boelhouwer JG, Piepers HW, Drinkenburg AAH. Nature and characteristics of pulsing flow in trickle-bed reactors. *Chemical Engineering Science.* 2002;57:4865-4876.
20. Shaban H, Tavoularis S. Measurement of gas and liquid flow rates in two-phase pipe flows by the application of machine learning techniques to differential pressure signals. *International Journal of Multiphase Flow.* 2014;67:106-117.
21. Taghavi M, Balakotaiah V. Gas hold-up and bubble behavior in an upflow packed bed column in the limit of low flow rate. *AIChE Journal.* 2019;65(8):e16624.

Table 1: Comparison of parameters between aircraft and ISS tests.

Parameter	**Range for Aircraft Tests**	**Range for ISS Tests**
L	3 – 50 kg/m^2.s	0.25 – 20 kg/ m^2.s
G	0.03 – 0.8 kg/m^2.s	4x10^{-4} – 0.14 kg/ m^2.s
Re^*_{LS}	10 – 455	1.5 – 105
Re^*_{GS}	13 - 265	0.1 - 33
Su_L	400 – 365,000	26,000
μ_L	0.001 – 0.02 kg/m.s	0.0009 kg/m.s
ε	0.34	0.34
d_P	0.002 – 0.005 m	0.003 m
σ	0.060 – 0.072 kg/s^2	0.065 – 0.070 kg/s^2
g	~ 0.02 m/s^2	10^{-4}m/s^2
Packing Materials	Glass and Alumina	Glass and Teflon

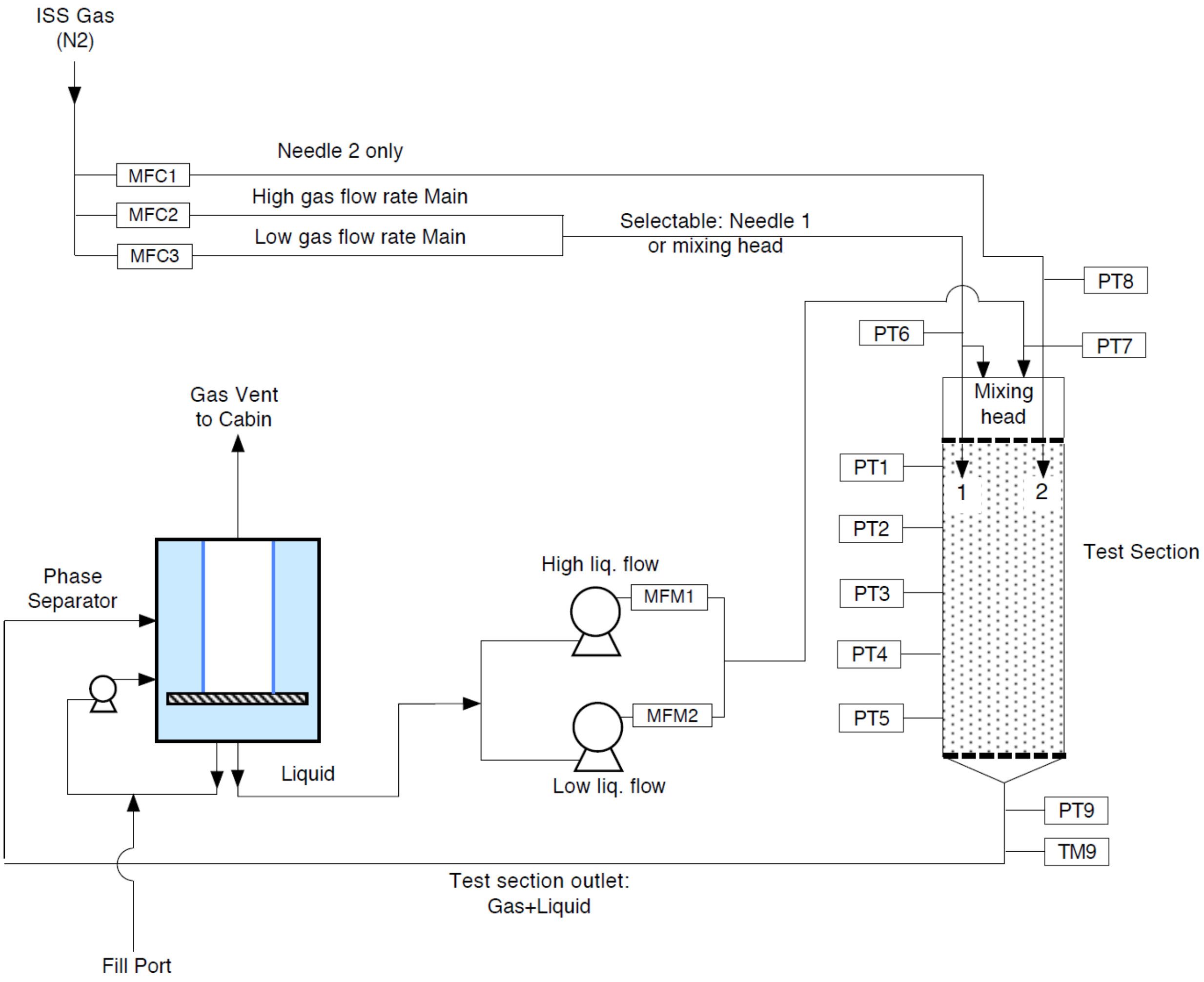
ISS Gas
(N2)
Needle 2 only
MFC1
High gas flow rate Main
MFC2
Low gas flow rate Main
MFC3
Selectable: Needle 1
or mixing head
PT8
PT6
PT7
Mixing
head
Gas Vent
to Cabin
PT1
1
2
PT2
Test Section
Phase
Separator
High liq. flow
MFM1
PT3
PT4
MFM2
PT5
Liquid
Low liq. flow
PT9
TM9
Test section outlet:
Gas+Liquid
Fill Port

Figure 1

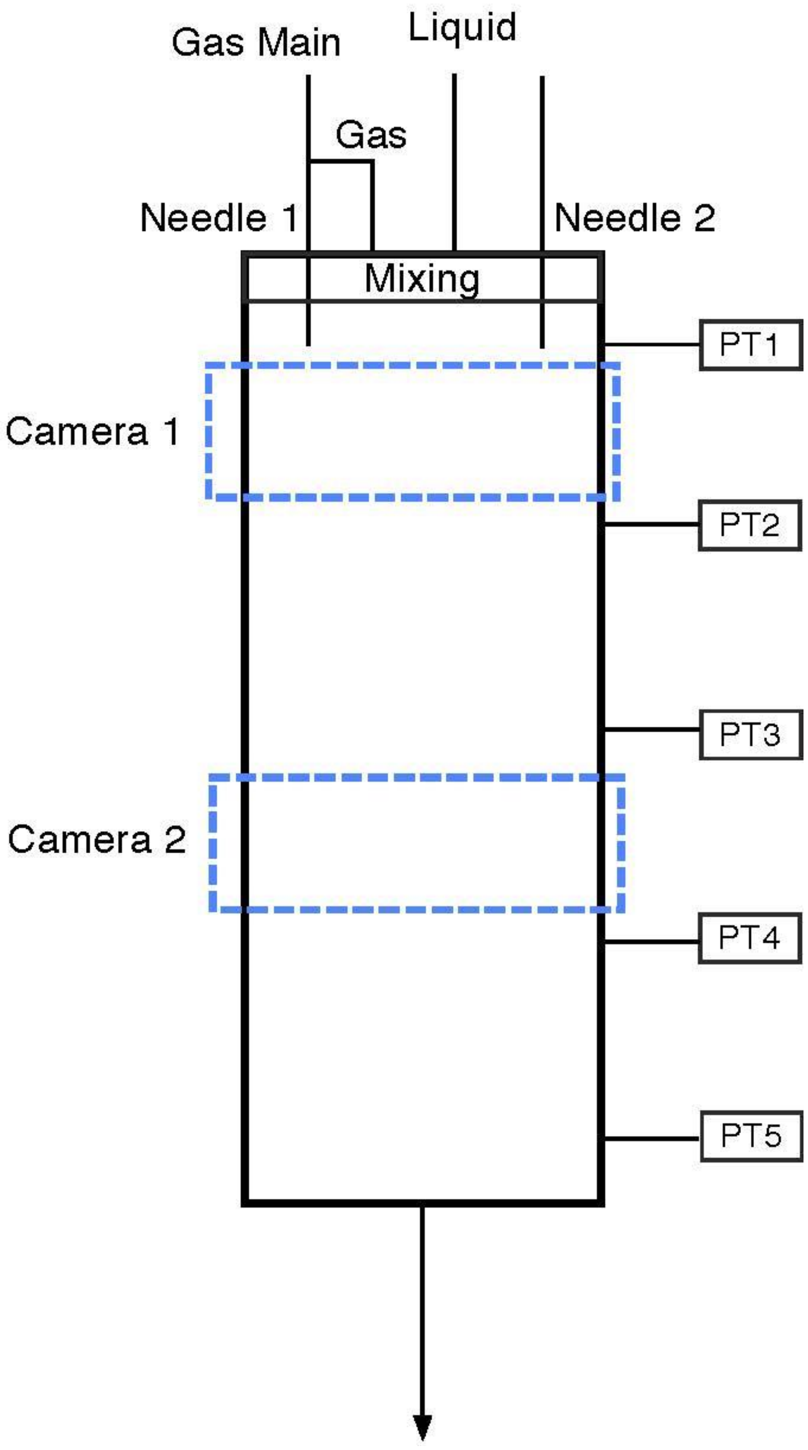
Gas Main
Liquid
Gas
Needle 1
Needle 2
Mixing
PT1
Camera 1
PT2
PT3
Camera 2
PT4
PT5

Figure 2

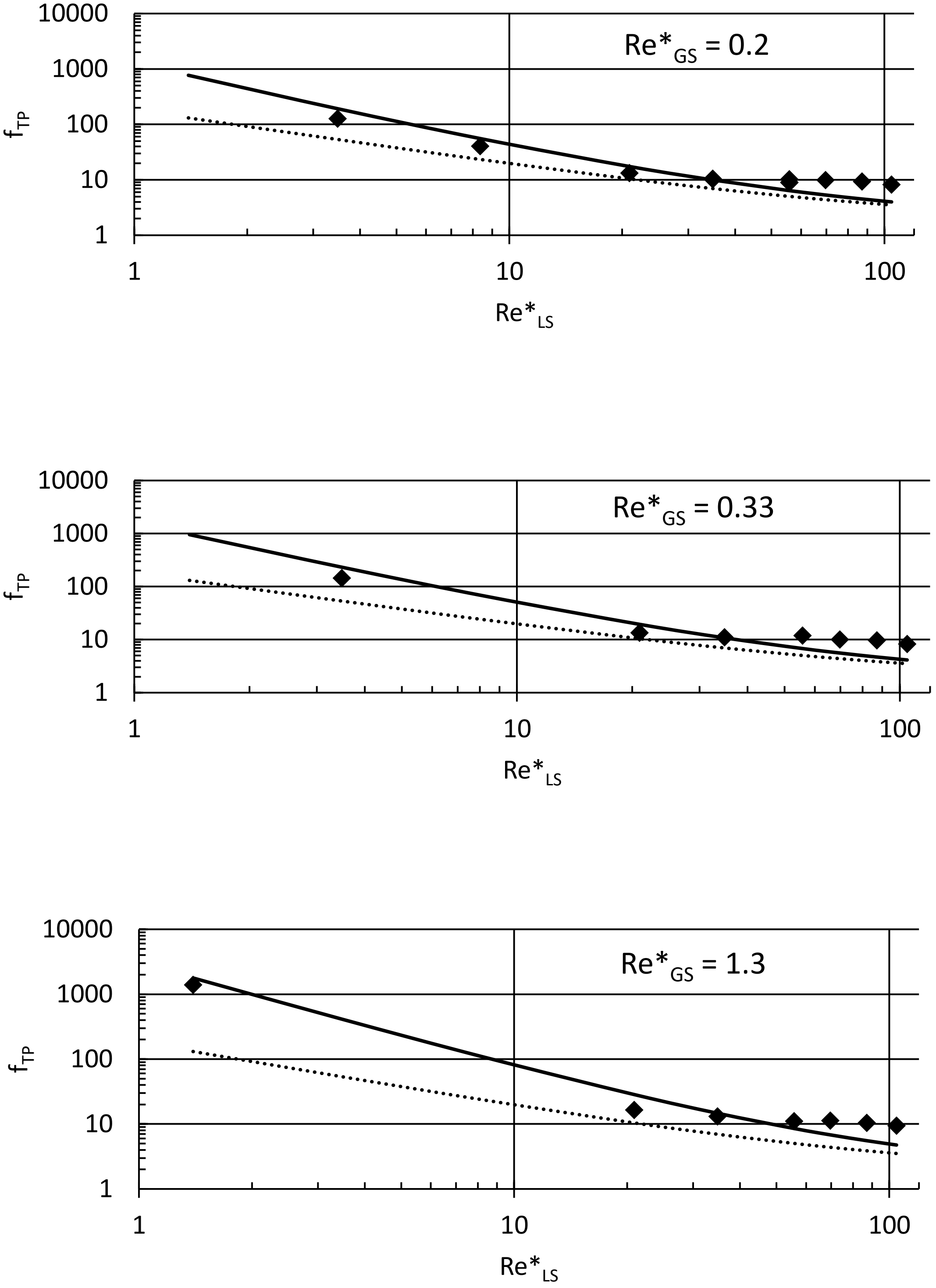10000
1000
100
10
1
f_TP
Re*_GS = 0.2
1
10
100
Re*_LS
10000
1000
100
10
1
f_TP
Re*_GS = 0.33
1
10
100
Re*_LS
10000
1000
100
10
1
f_TP
Re*_GS = 1.3
1
10
100
Re*_LS

Figure 3

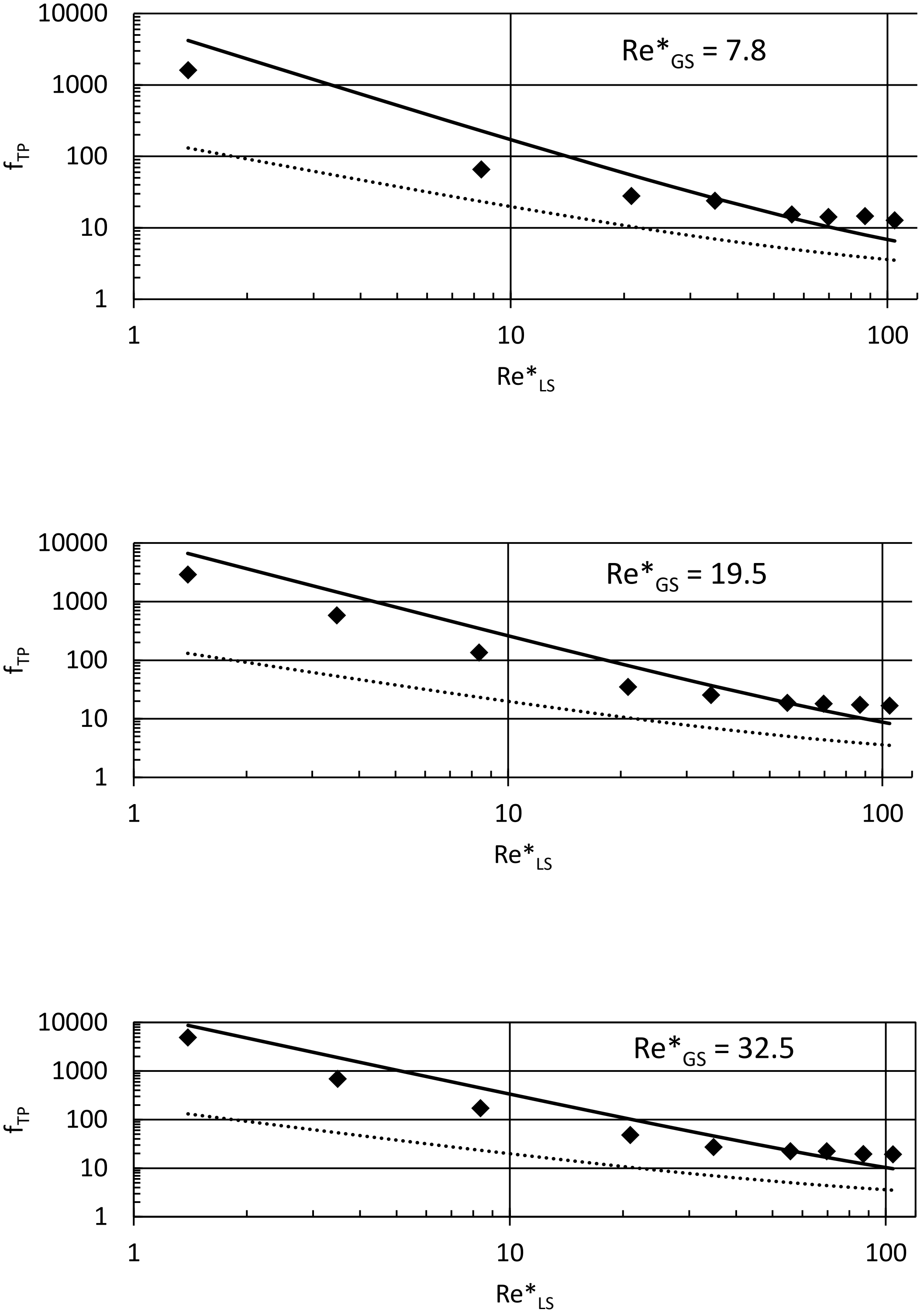
Re*$_{GS}$ = 7.8
f$_{TP}$
10000
1000
100
10
1
1
10
100
Re*$_{LS}$
Re*$_{GS}$ = 19.5
f$_{TP}$
10000
1000
100
10
1
1
10
100
Re*$_{LS}$
Re*$_{GS}$ = 32.5
f$_{TP}$
10000
1000
100
10
1
1
10
100
Re*$_{LS}$

Figure 4

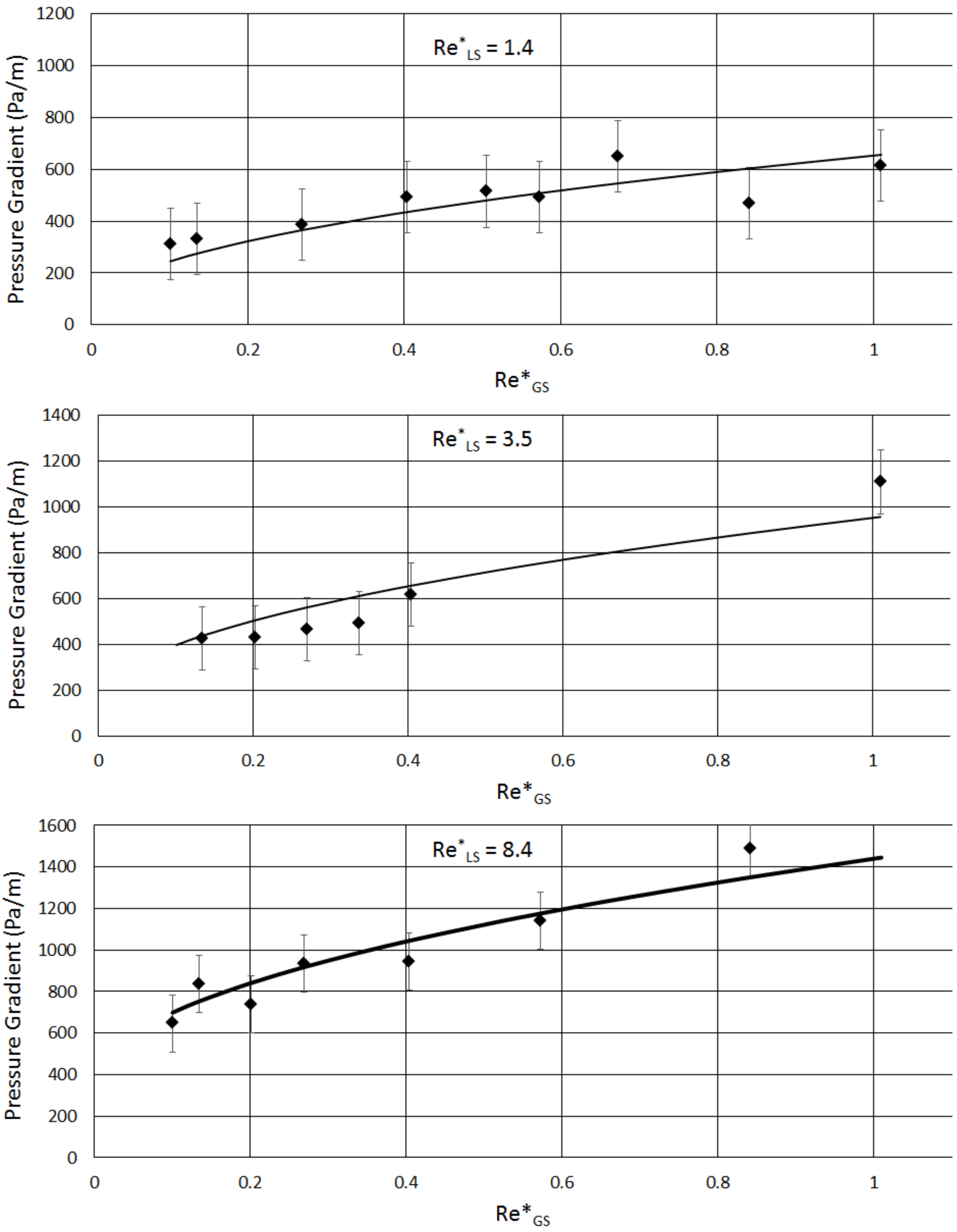
Re*_LS = 1.4
Pressure Gradient (Pa/m)
0
200
400
600
800
1000
1200
0
0.2
0.4
0.6
0.8
1
Re*_GS
Re*_LS = 3.5
Pressure Gradient (Pa/m)
0
200
400
600
800
1000
1200
1400
0
0.2
0.4
0.6
0.8
1
Re*_GS
Re*_LS = 8.4
Pressure Gradient (Pa/m)
0
200
400
600
800
1000
1200
1400
1600
0
0.2
0.4
0.6
0.8
1
Re*_GS

Figure 5

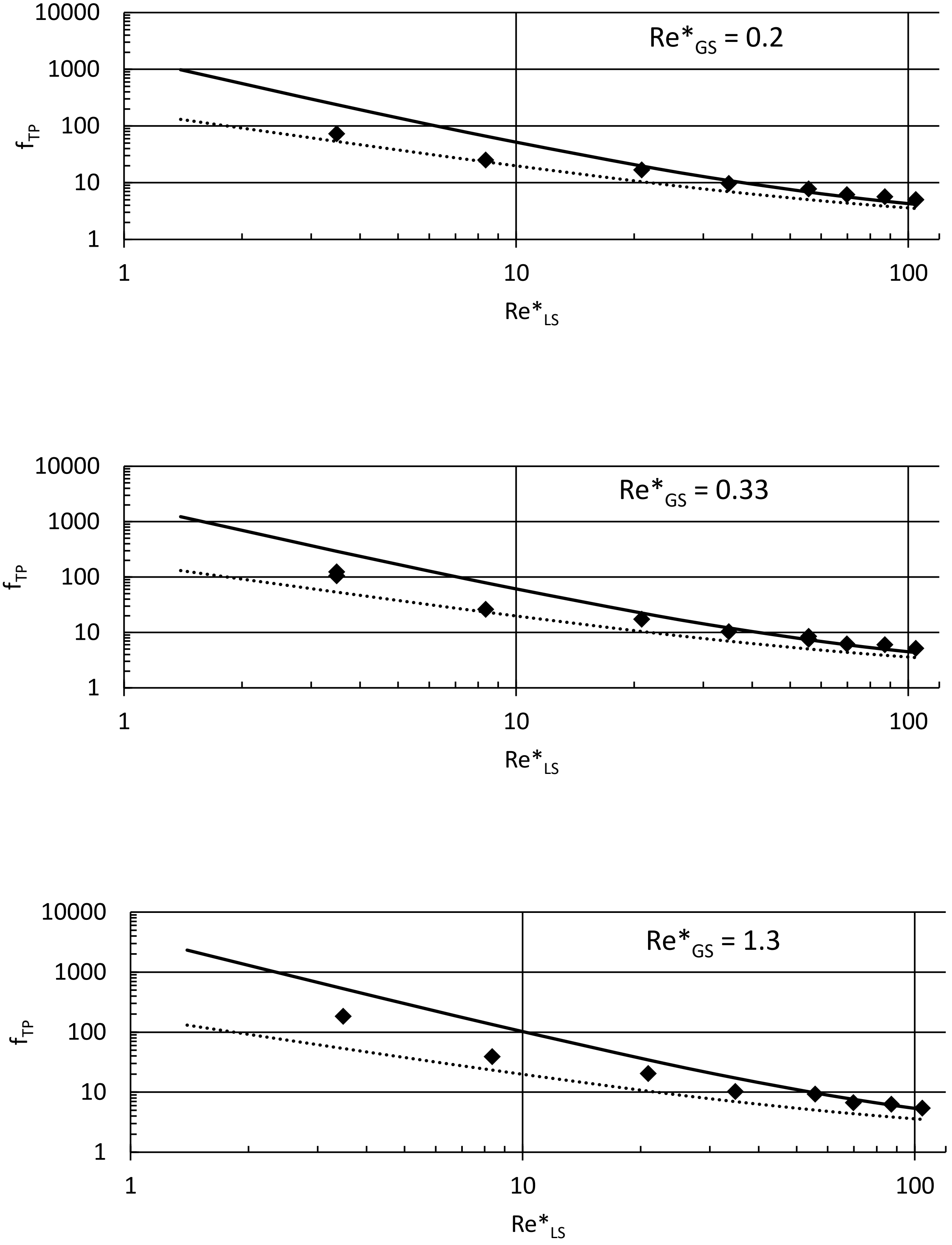

Figure 6

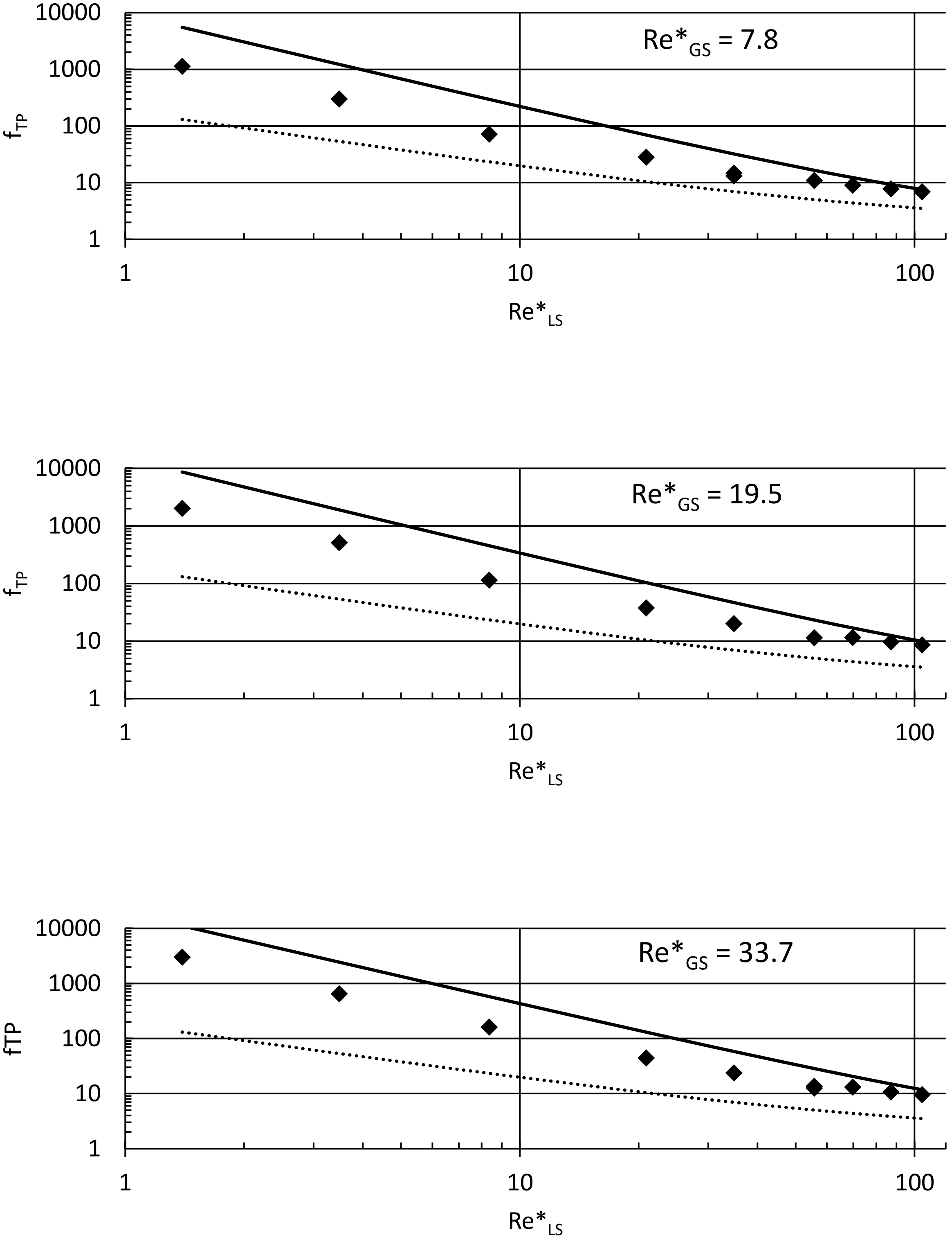
10000
1000
100
10
1
f_{TP}
1
10
100
Re^*_{LS}
Re^*_{GS} = 7.8
10000
1000
100
10
1
f_{TP}
1
10
100
Re^*_{LS}
Re^*_{GS} = 19.5
10000
1000
100
10
1
fTP
1
10
100
Re^*_{LS}
Re^*_{GS} = 33.7

Figure 7

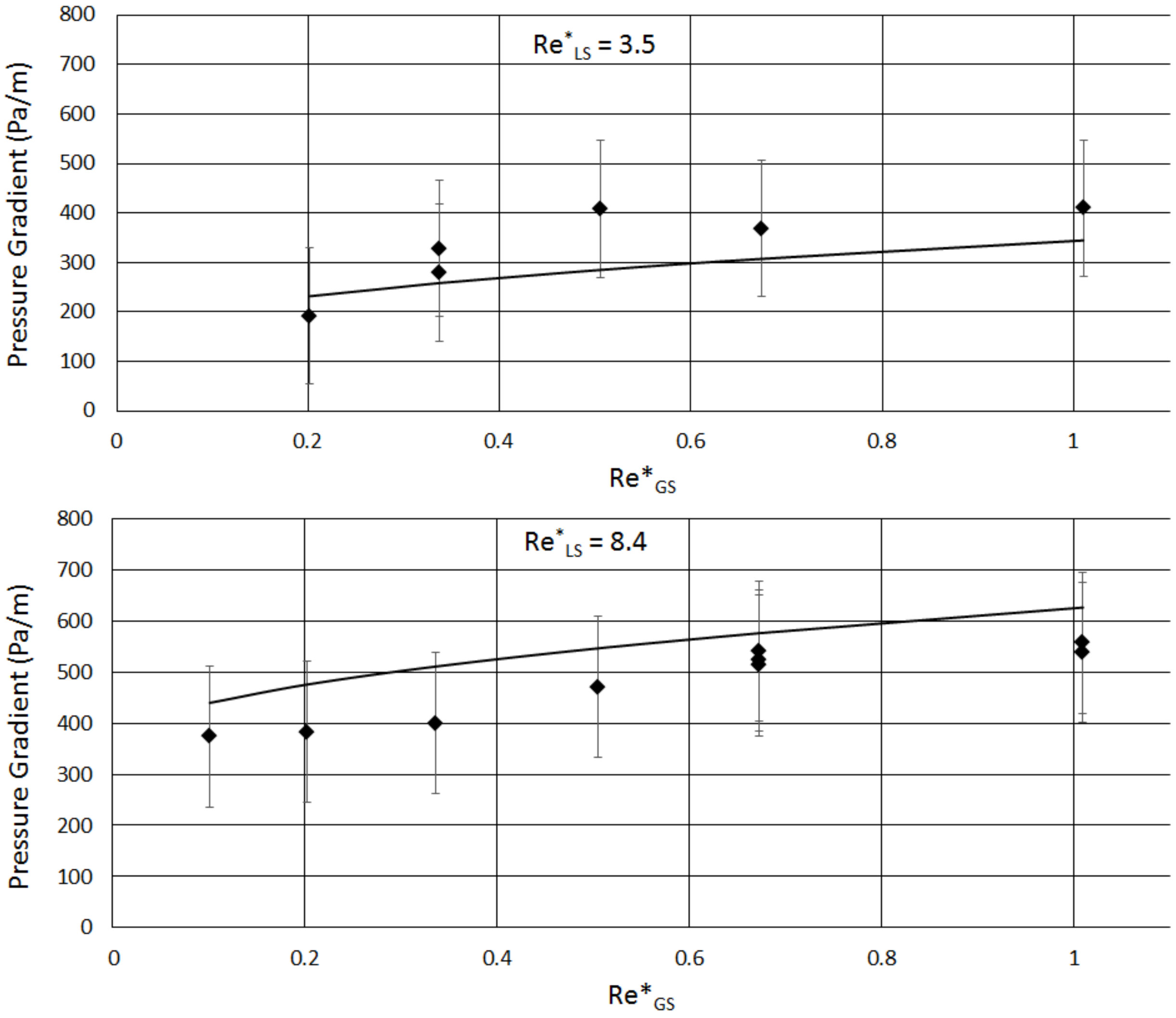
Re*$_{LS}$ = 3.5
Pressure Gradient (Pa/m)
800
700
600
500
400
300
200
100
0
0
0.2
0.4
0.6
0.8
1
Re*$_{GS}$
Re*$_{LS}$ = 8.4
Pressure Gradient (Pa/m)
800
700
600
500
400
300
200
100
0
0
0.2
0.4
0.6
0.8
1
Re*$_{GS}$

Figure 8

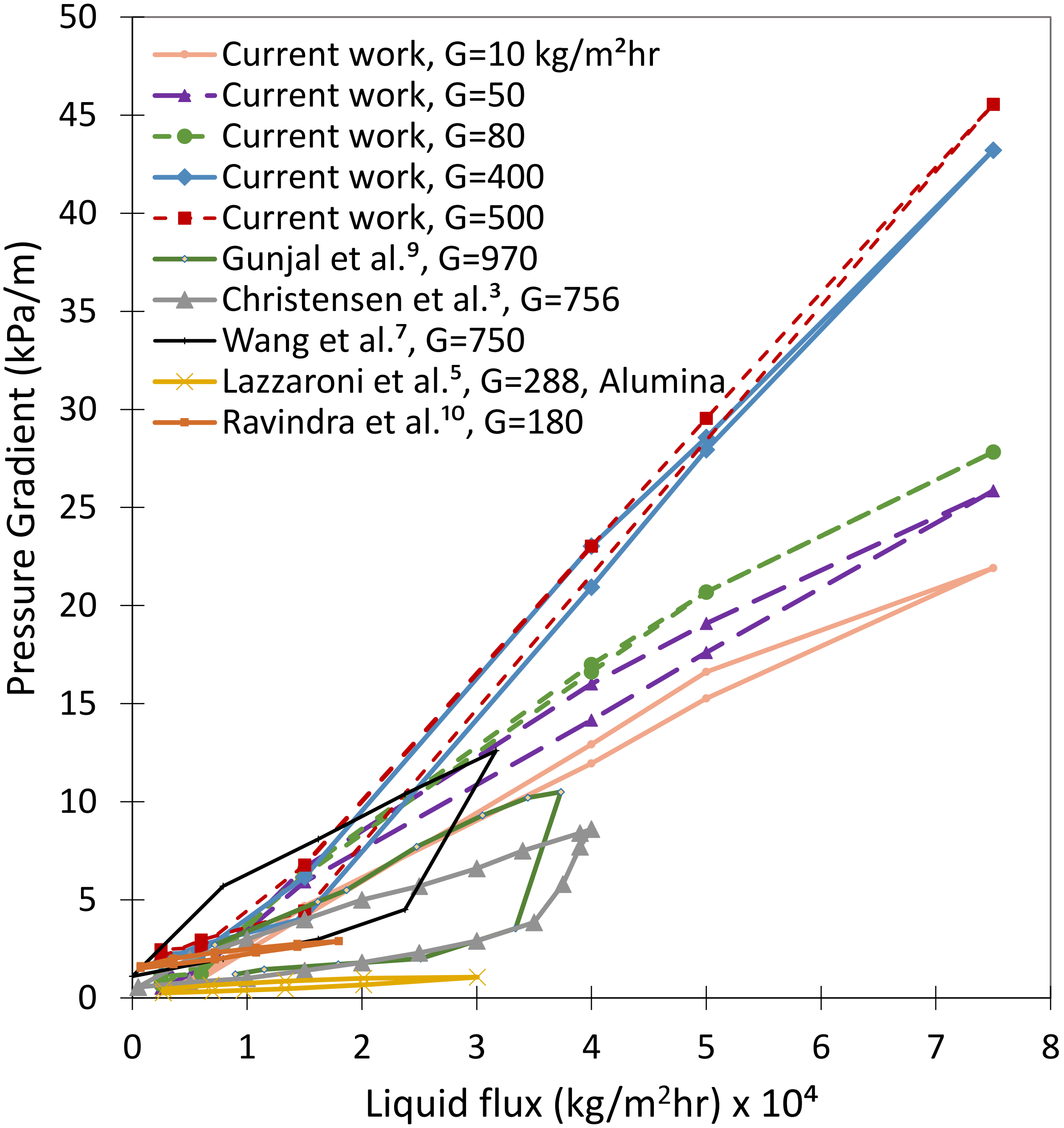
Pressure Gradient (kPa/m)
Liquid flux (kg/m²hr) x 10⁴
0
5
10
15
20
25
30
35
40
45
50
0
1
2
3
4
5
6
7
8
Current work, G=10 kg/m²hr
Current work, G=50
Current work, G=80
Current work, G=400
Current work, G=500
Gunjal et al.⁹, G=970
Christensen et al.³, G=756
Wang et al.⁷, G=750
Lazzaroni et al.⁵, G=288, Alumina
Ravindra et al.¹⁰, G=180

Figure 9

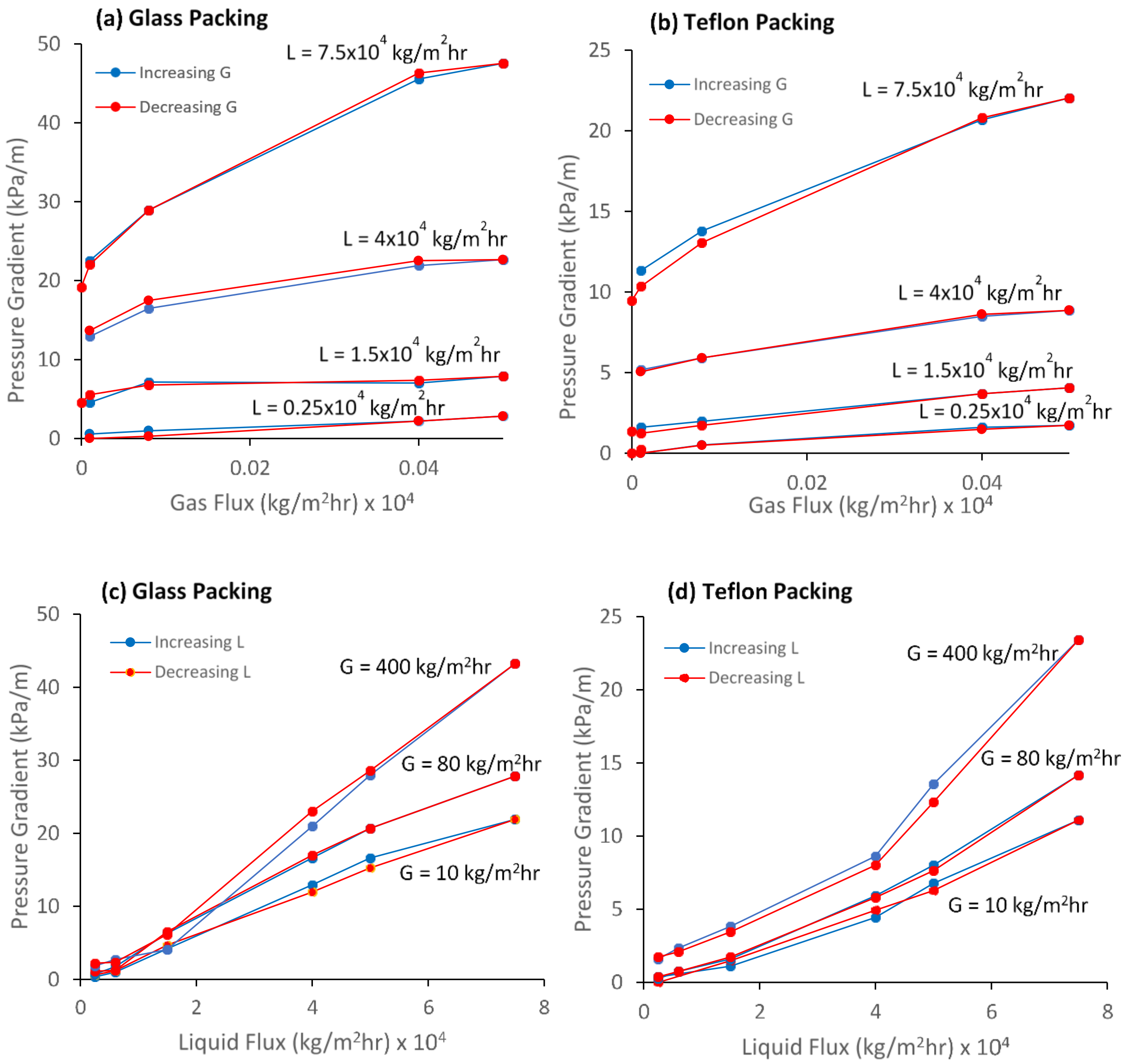
(a) Glass Packing
Pressure Gradient (kPa/m)
50
40
30
20
10
0
Increasing G
Decreasing G
L = 7.5x10⁴ kg/m²hr
L = 4x10⁴ kg/m²hr
L = 1.5x10⁴ kg/m²hr
L = 0.25x10⁴ kg/m²hr
0
0.02
0.04
Gas Flux (kg/m²hr) x 10⁴
(b) Teflon Packing
Pressure Gradient (kPa/m)
25
20
15
10
5
0
Increasing G
Decreasing G
L = 7.5x10⁴ kg/m²hr
L = 4x10⁴ kg/m²hr
L = 1.5x10⁴ kg/m²hr
L = 0.25x10⁴ kg/m²hr
0
0.02
0.04
Gas Flux (kg/m²hr) x 10⁴
(c) Glass Packing
Pressure Gradient (kPa/m)
50
40
30
20
10
0
Increasing L
Decreasing L
G = 400 kg/m²hr
G = 80 kg/m²hr
G = 10 kg/m²hr
0
2
4
6
8
Liquid Flux (kg/m²hr) x 10⁴
(d) Teflon Packing
Pressure Gradient (kPa/m)
25
20
15
10
5
0
Increasing L
Decreasing L
G = 400 kg/m²hr
G = 80 kg/m²hr
G = 10 kg/m²hr
0
2
4
6
8
Liquid Flux (kg/m²hr) x 10⁴

Figure 10

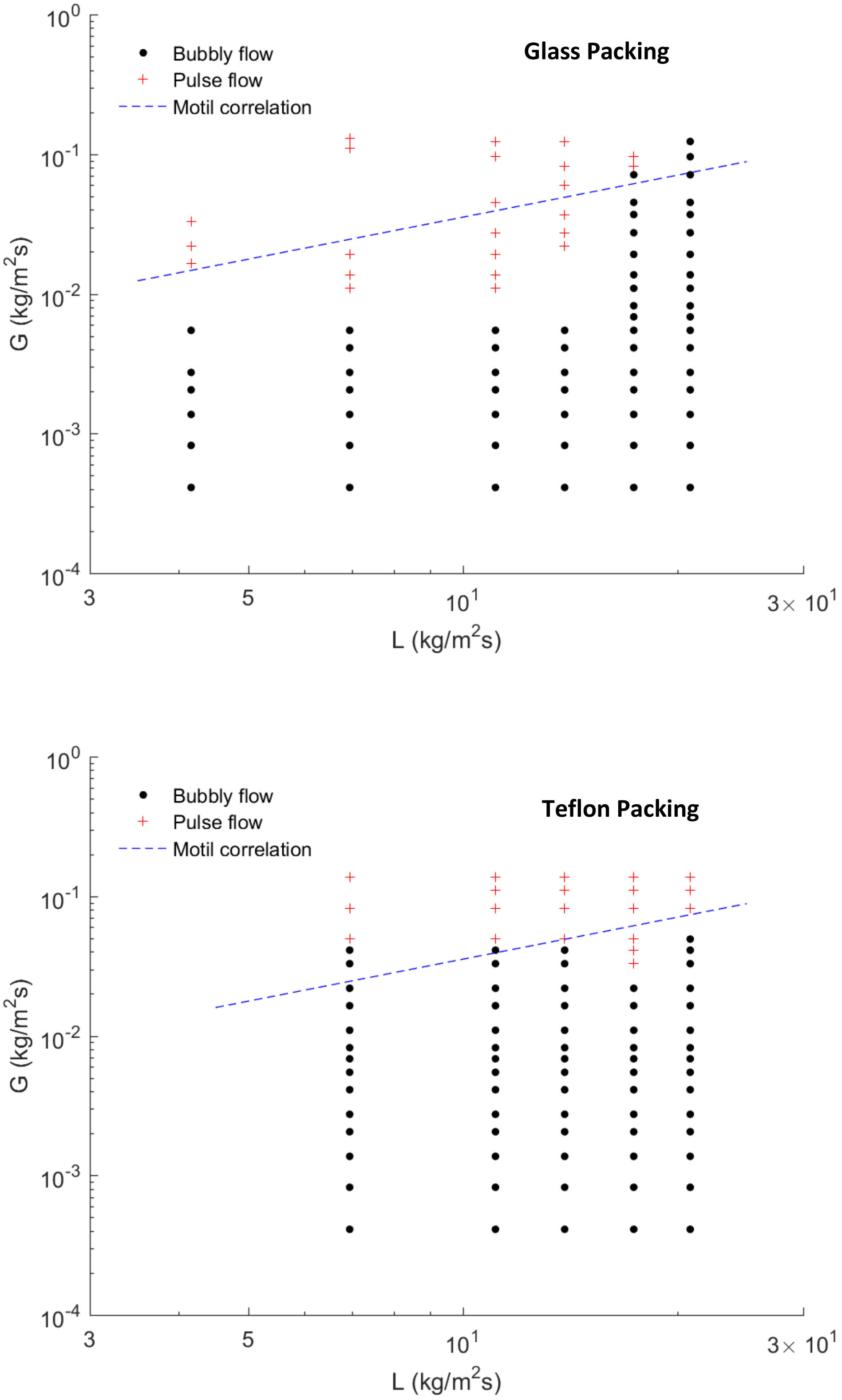
Glass Packing
● Bubbly flow
+ Pulse flow
- - - Motil correlation
G (kg/m²s)
10^0
10^-1
10^-2
10^-3
10^-4
3
5
10^1
3× 10^1
L (kg/m²s)
Teflon Packing
● Bubbly flow
+ Pulse flow
- - - Motil correlation
G (kg/m²s)
10^0
10^-1
10^-2
10^-3
10^-4
3
5
10^1
3× 10^1
L (kg/m²s)

Figure 11

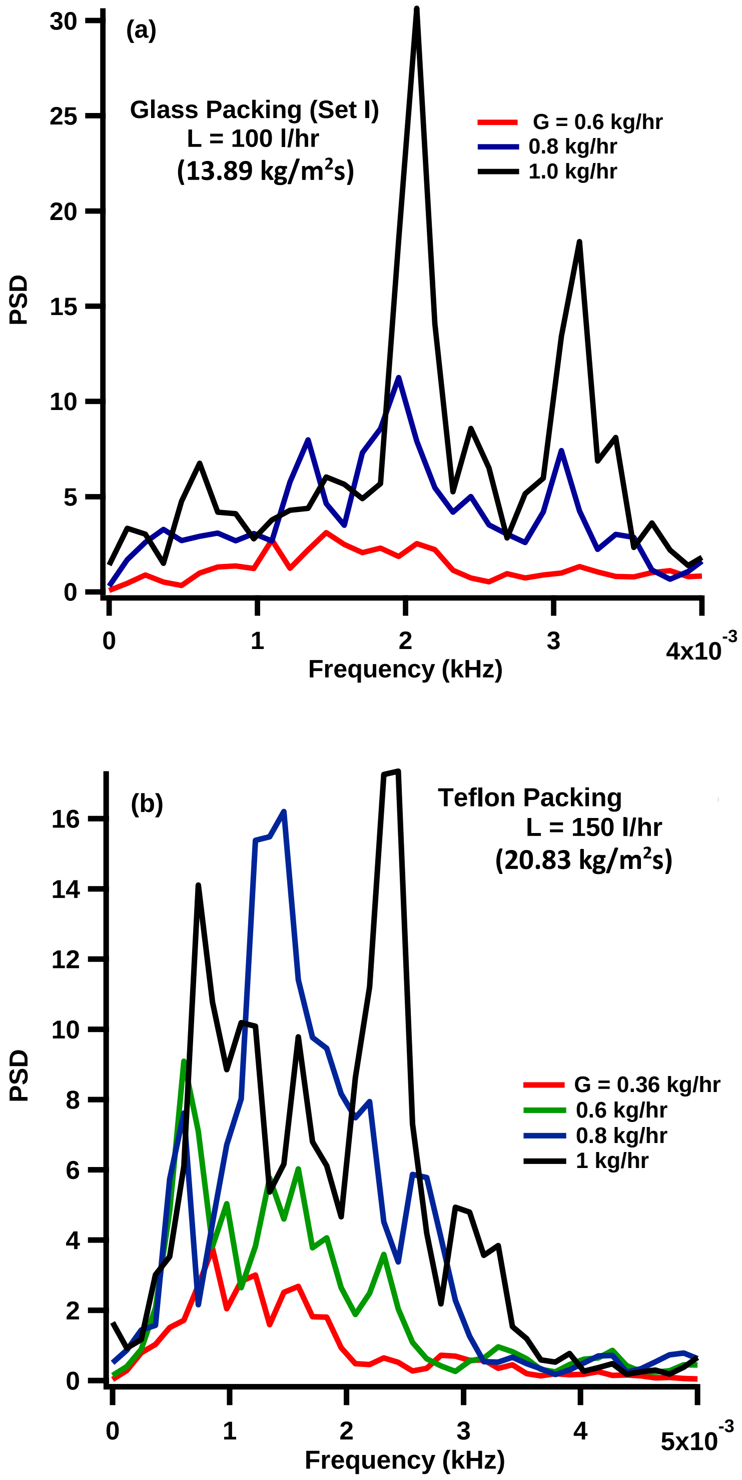
(a)
Glass Packing (Set I)
L = 100 l/hr
(13.89 kg/m²s)
G = 0.6 kg/hr
0.8 kg/hr
1.0 kg/hr
PSD
30
25
20
15
10
5
0
0
1
2
3
4x10⁻³
Frequency (kHz)
(b)
Teflon Packing
L = 150 l/hr
(20.83 kg/m²s)
G = 0.36 kg/hr
0.6 kg/hr
0.8 kg/hr
1 kg/hr
PSD
16
14
12
10
8
6
4
2
0
0
1
2
3
4
5x10⁻³
Frequency (kHz)

Figure 12